Original Research Article

Riser Configuration Design for a 15-MW Floating Offshore Wind Turbine Integrated with a Green Hydrogen Facility

Sung-Jae Kim[1] and Sung-Ju Park[2,3]

[1]*Researcher, Fisheries Engineering Division, National Institute of Fisheries Science, Busan, Republic of Korea*
[2]*Assistant Professor, School of Electrical & Control Engineering, Tongmyong University, Busan, Republic of Korea*
[3]*Researcher, Open Grid Laboratory, Busan, Republic of Korea*

ABSTRACT: *Green hydrogen presents a sustainable and environmentally friendly solution for clean energy production and transportation. This study aims to identify the optimal profile of green hydrogen transportation risers originating from a floating offshore wind turbine (FOWT) integrated with a hydrogen production facility. Employing the Cummins equation, a fully coupled dynamic analysis for FOWT with a flexible riser was conducted, with the tower, mooring lines, and risers described using a lumped mass line model. Initially, motion response amplitude operators (RAOs) were compared with openly published results to validate the numerical model for the FOWT. Subsequently, a parametric study was conducted on the length of the buoyancy module section and the upper bare section of the riser by comparing the riser's tension and bending moment. The results indicated that as the length of the buoyancy module increases, the maximum tension of the riser decreases, while it increases with the lengthening of the bare section. Furthermore, shorter buoyancy modules are expected to experience less fatigue damage, with the length of the bare section having a relatively minor impact on this phenomenon. Consequently, to ensure safety under extreme environmental conditions, both the upper bare section and the buoyancy module section should be relatively short.*

1. Introduction

To address climate change resulting from rising global temperatures, there is a growing worldwide interest in achieving net-zero carbon emissions. In response, the European Union (EU) aims to establish a hydrogen economy through its 2020 Hydrogen Strategy, which secures renewable hydrogen-related technologies across various sectors, including industry and transportation. By 2030, the EU plans to develop a 40 GW electrolysis facility and produce 10 million tons of green hydrogen (European Commission, 2020). Renewable hydrogen is categorized into green, blue, and gray hydrogen based on the amount of greenhouse gases emitted during production. Green hydrogen, produced from renewable energy without greenhouse gas emissions, has a higher production cost compared to other hydrogen types, but is increasingly recognized as a clean energy solution with international environmental regulations becoming stricter (Martinez-Luengo et al., 2017; Yu et al., 2021). Offshore wind, characterized by long full load hours and stronger winds compared to land-based systems, is classified as a valuable resource for green hydrogen production.

Research is being conducted on infrastructure design and economic evaluation for hydrogen production (Pham et al., 2021).

Offshore wind turbines can generally be categorized into fixed and floating types based on water depth. Offshore fixed wind turbines are typically used in water depths of less than 60 m, while floating structures are cost-effective in areas deeper than 100 m. Floating wind turbines, installed in areas with stronger offshore winds, can support large, heavy turbines without concerns about the seabed utilizing self-buoyancy. Eurek et al. (2017) indicate that 80% of global offshore wind resources are located in deep waters (over 60 m), suggesting the potential for large-scale floating offshore wind turbines to operate alongside green hydrogen production platforms. The National Renewable Energy Laboratory (NREL) in the United States, in collaboration with the University of Maine, has developed the Volturn US-S semi-submersible platform for a 15 MW wind turbine as part of the International Energy Agency (IEA) Wind Energy 37 initiative (Allen et al., 2020). Various studies utilizing this floating wind turbine platform have been conducted. For instance, Pillai et al. (2022) enhanced the mooring footprint to reduce loads by optimizing the

anchoring of the IEA 15 MW turbine and VolturnUS-S platform through numerical simulations in shallow water. Niranjan and Ramisetti (2022) conducted a fully coupled dynamic analysis for the IEA 15 MW wind turbines and VolturnUS-S platforms based on aero-hydro-servo-elastic codes. Additionally, Balli and Zheng (2022) proposed a pseudo-coupling approach to simplify the fatigue damage evaluation procedures for semi-submersible offshore wind turbines. Further research on various forms of floating wind turbine platforms is also being conducted. Heo et al. (2023) reviewed the safety of the supporting structures of an 8−10 MW Tri-Star floating wind turbine under operating environmental conditions and extreme environmental conditions. Jin et al. (2023) applied the effective inertia coefficient technique to reduce the computational time for the OC4 semi-submersible platform.

Methods for integrating floating offshore wind turbines (FOWTs) with green hydrogen production facilities include transmitting electricity generated from the wind turbines via cables to onshore or offshore hydrogen production facilities, or equipping hydrogen production facilities on the floating wind turbine platform to produce green hydrogen using the generated electricity and then transmitting it via risers and pipes (Ibrahim et al., 2023). The first method requires producing high-voltage current to minimize energy losses and delivering the generated electrical energy to the hydrogen production facilities. In contrast, the second method has the advantage of using proven risers and pipes commonly used in marine engineering to produce and transport green hydrogen with minimal energy loss. To apply the second method, research into the design of green hydrogen risers for floating wind turbines is essential. However, studies on the coupled analysis between these floating wind turbines and risers are nearly nonexistent. Therefore, prior research related to the design of offshore risers for oil production and transportation should be referenced for configuring green hydrogen risers and pipes. Recent relevant studies include Li et al. (2016), who conducted a basic configuration design for a flexible riser in a turret-moored floating production storage offloading (FSPO) vessel in the South China Sea, comparing tension and curvature. Trapper (2020) also used a simplified structural analysis model to design the riser configuration so that the lazy wave flexible riser would have minimal potential energy. Additionally, Elsas et al. (2021) estimated the optimal configuration of the riser using Bayesian optimization methods.

The objective of this study is to determine the optimal configuration of a hydrogen riser for a green hydrogen transportation from a 15-MW floating wind turbine to onshore. Specifically, a validated floating wind turbine model was used to analyze the global motion of the floating platform under extreme loading conditions, and to assess the hydrodynamic performance and safety of the mooring lines and lazy wave riser. The location and length of the buoyancy module of the riser were estimated using a parametric study. In this context, the tension and bending moment of the riser were compared to determine the optimal riser configuration, and these were analyzed using response surface methods.

2. Dynamics of 15-MW FOWT with Green Hydrogen

For hydrodynamic analysis of the floating wind turbine platform, it is necessary to consider the coupling effects among the floating body, mooring system, tower, and turbine. This requires analyzing the hydrodynamics of the floating body, the elastodynamics of the mooring system and tower, and the aerodynamics of the turbine, and an integrated dynamic analysis model must be constructed. Additionally, in the dynamic analysis model, the energy efficiency of floating offshore wind turbines can be maximized through control of the blade pitch or yaw angle of wind turbines. In this study, since the focus is on evaluating the safety of the green hydrogen riser of floating wind turbines under extreme environmental conditions, the control strategy of the wind turbine blades were not considered. Therefore, the equations of motion for the floating body of wind turbines can be expressed as follows:

$$(M + M_a(\infty))\ddot{\xi}(t) + C\dot{\xi}(t) + K\xi(t)$$
$$= F_{w1}(t) + F_{w2}(t) + F_C(t) + F_M(t) + F_{Tower}(t) \tag{1}$$

where M, $M_a(\infty)$, C, and K denote the mass matrix of the floating body, added mass matrix at infinite frequency, additional damping matrix considering viscous effects, and the restoring coefficient matrix based on the wetted surface of the floating body, respectively. The additional damping matrix can be defined in the form of a quadratic damping force proportional to the square of the floating body's velocity. F_{w1}, F_{w2}, F_C, F_M, and F_{Tower} denote the matrices for the wave-frequency wave force, second-order wave force, radiated damping force matrix owing to the floating body's radiation force, mooring force matrix from the coupling effect due to the mooring lines and risers, and the load matrix owing to the tower's elasticity, respectively. ξ, $\dot{\xi}$, and $\ddot{\xi}$ denote the displacement, velocity, and acceleration matrices of the floating body's motion, respectively, with the motion of the floating body having six degrees of freedom, comprising three translational motions (surge, sway, and heave) and three rotational motions (roll, pitch, and yaw). The wave-frequency wave force, second-order wave force, and radiated damping force can be expressed as Eqs. (2), (3), and (4), respectively:

$$F_{w1}(t) = Re\left[\sum_{j=1}^{N_w} A_j L(\omega_j) e^{-i\omega j t}\right] \tag{2}$$

$$F_{w2}(t) = Re\left[\sum_{j=1}^{Nw} \sum_{k=1}^{Nw} A_j A_k^* D(\omega_j, -\omega_k) e^{-i(w_j - w_k)t}\right] \tag{3}$$

$$F_C(t) = -\int_0^t R(\tau - t)\dot{\xi}(\tau) d\tau \tag{4}$$

where w_j and A_j represent the wave frequency and incident wave amplitude at the j-th frequency component, respectively, and N_w
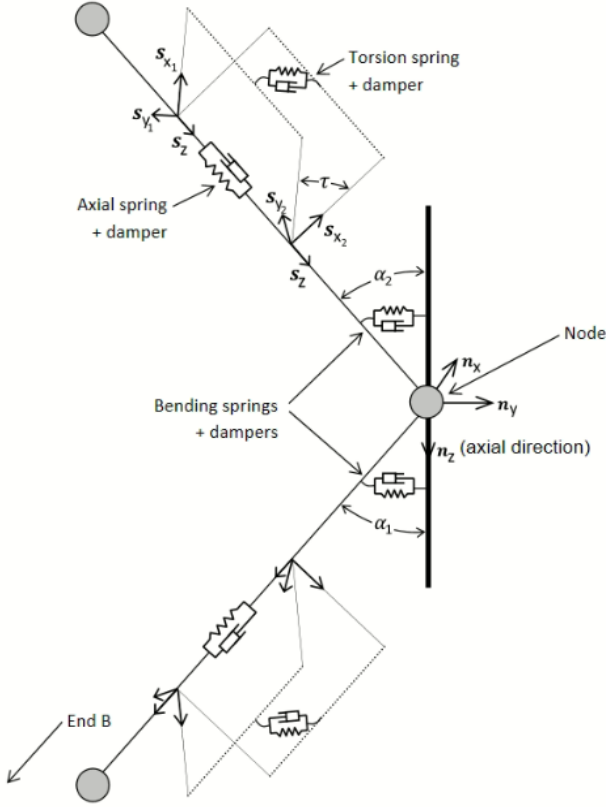
Fig. 1 Lumped mass line model (Orcina, 2023)

denotes the number of frequency components of the incident wave. In this study, irregular wave conditions were described based on 300 incident wave frequency components. $L(w)$ and $D(\omega_1, \omega_2)$ represent the linear transfer function of the wave-frequency wave load and the quadratic transfer function of the low-frequency wave load, respectively. In this study, the Newman approximation was applied to represent the low-frequency wave load. $R(t)$ denotes the impulse response function of the radiation force, which is defined through the Fourier cosine transform of the radiation damping coefficient. The wave-frequency and second-order wave loads and radiation damping coefficient were obtained by solving diffraction and radiation problems.

Submerged line structures (such as mooring lines and risers), as well as offshore wind turbine towers and blades, can all be represented using a lumped-mass model. In this model, relatively slender objects are represented as a series of elements, with two nodes at each end of an element accounting for half of the element mass. These nodes are connected by axial stiffness and damping, bending stiffness and damping, and torsional stiffness and damping (see Fig. 1). The stiffness of each component is influenced by the material properties and the structural dimensions of the materials. Additionally, submerged line structures, along with the tower and turbine blades, are affected by fluid flow drag under environmental loads (Eq. 5), and the submerged line structures are subject to added mass proportional to the object's acceleration due to the surrounding water (Eq. 6). These are expressed as follows:

$$F_D = \frac{1}{2}\rho Dl C_D v|v| \tag{5}$$

$$F_A = C_M \Delta a_f - C_a \Delta a_r \tag{6}$$

where ρ, D, l, and Δ denote the fluid density, object diameter, element length, and element mass, respectively. C_M, C_a, and C_D represent the matrices representing the inertia coefficient, added mass coefficient, and drag coefficient, respectively, and v, a_f, and a_r are the relative velocity between fluid and elements, fluid acceleration, and element acceleration, respectively. By applying these two environmental loads to a lumped-mass model shown in Fig. 1, the behavior and loads of the mooring lines, risers, tower, and turbine blades can be calculated.

3. Numerical Analysis Model

3.1 15-MW FOWT Platform

This study utilized the IEA-15-240 RWT 15-MW turbine and the semi-submersible platform VolturnUS-S (Allen et al., 2020). The IEA-15-240 RWT 15-MW turbine is a conventional horizontal-axis turbine with three blades, a rotor diameter of 240 m, a hub height of 150 m, and an operating wind speed range of 3−25 m/s. Developed by the NREL and the University of Maine, the VolturnUS-S comprises four columns, as shown in Fig. 2, with the wind turbine connected to the central column. Detailed specifications are presented in Table 1. The numerical model of the floating platform is represented by a total of 3,508 rectangular elements.

The floating wind turbine uses three mooring lines to maintain its position, as shown in Fig. 3, with each mooring line being connected to an outer column and installed at 120° intervals. Each mooring line comprises an R3 studless chain with a nominal diameter of 185 mm. The total length of the mooring line is 850 m, with a horizontal distance from the floating platform to the anchor of 837.6 m. The minimum breaking load of the mooring line was 22,286 kN. The added mass coefficient and drag coefficient were referenced from

Table 1 Property specifications of the VolturnUS-S platform (Allen et al., 2020)

Parameter	Value
Hull displacement (m³)	20,206
Hull steel mass (t)	3.914
Tower interface mass (t)	100.0
Ballast (fixed/fluid) (t)	2.54/11.30
Design draft (m)	20.0
Freeboard (m)	14.0
Vertical center of gravity from still water line (m)	−14.94
Vertical center of buoyancy from still water line (m)	−13.63
Roll inertia about the center of gravity (kg·m²)	1.251×10^{10}
Pitch inertia about the center of gravity (kg·m²)	1.251×10^{10}
Yaw inertia about the center of gravity (kg·m²)	2.367×10^{10}
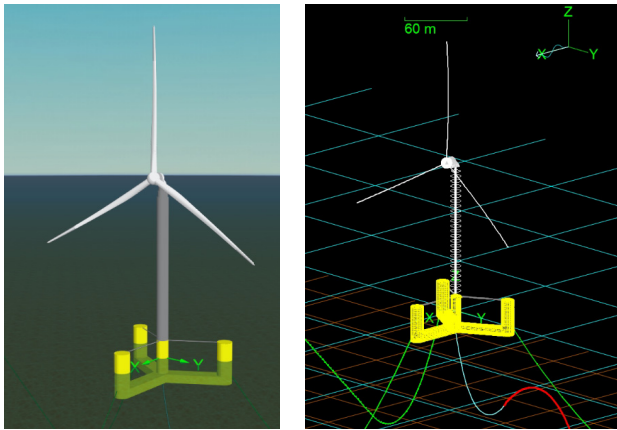
(a) Illustration (b) Numerical model

Fig. 2 Configuration of 15-MW floating offshore wind turbine

DNVGL-RP-C205 (DNV GL, 2021a) and DNVGL-OS-301 (DNV GL, 2021b). Further details are presented in Table 2.

3.2 Green Hydrogen Riser

Risers and pipes for transporting green hydrogen can directly utilize those widely employed in ocean engineering field, which have already been validated for their safety and durability. A scenario was set where energy produced through wind power is converted into green hydrogen and transported via a riser. The numerical model for the green hydrogen riser used the lazy wave riser model provided as an example in OrcaFlex. This model applies a flexible joint at the connection between the floating structure and the riser, with a buoyancy module installed in the middle to represent the lazy wave riser shape (Fig. 4). A parametric study was conducted by adjusting the length and position
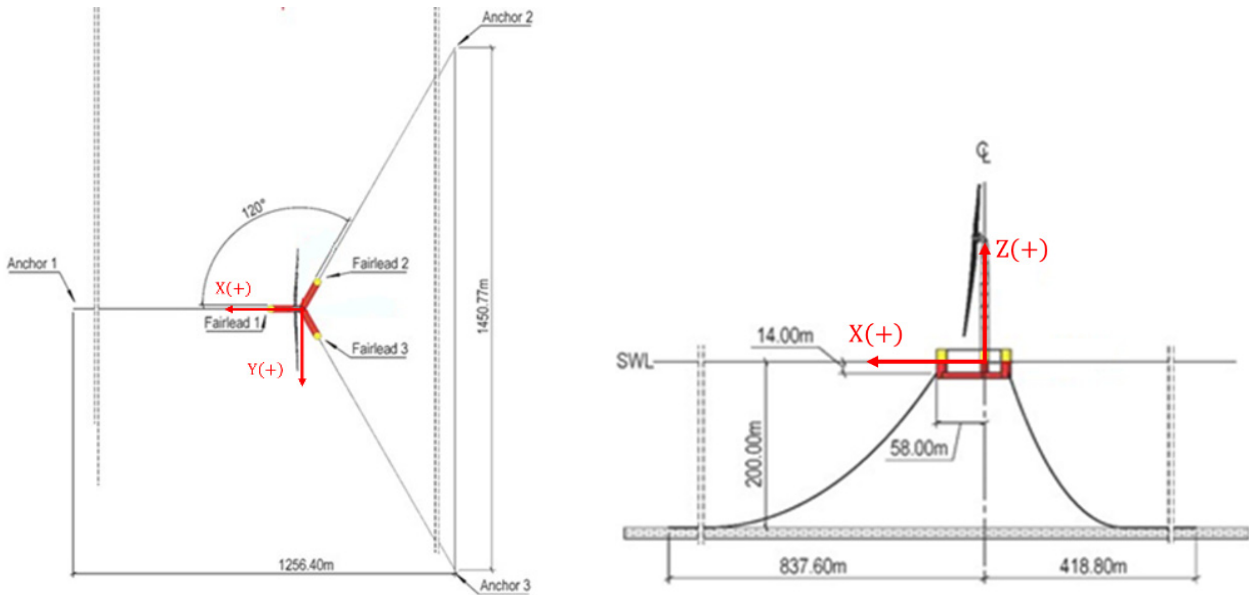

Fig. 3 Overview of the mooring system for 15-MW floating offshore wind turbine (Allen et al. 2020)

Table 2 Mooring system properties of the VolturnUS-S platform (Allen et al., 2020)

Parameter	Value
Line breaking strength (kN)	22,286
Anchor depth from M.W.L. (m)	200
Fairlead depth from M.W.L. (m)	14
Anchor radial spacing (m)	837.6
Fairlead radial spacing (m)	58
Nominal chain diameter (m)	0.185
Dry line linear density (kg/m)	685
Extensional stiffness (MN)	3270
Line unstretched length (m)	850
Fairlead pretension (kN)	2,437
Normal added mass coefficient	1.0
Tangential added mass coefficient	1.0
Normal drag coefficient	2.0
Tangential drag coefficient	1.15

Table 3 Specifications of flexible production riser from OrcaFlex examples (Orcina, 2023)

| Item	Parameter	Value
	Outer diameter (m)	0.3048
	Inner diameter (m)	0.254
	Young's Modulus (kPa)	216×10^6
	Poisson ratio	0.3
Bare part	Bending stiffness (kN·m^2)	46.5×10^3
	Axial stiffness (kN)	4.727×10^6
	Torsional stiffness (kN·m^2)	35.7×10^3
	Added mass coefficient	1.0
	Drag coefficient	0.008
	Outer diameter (m)	0.67929
Buoyancy part	Inner diameter (m)	0.2479
	Added mass coefficient	0.59827
	Drag coefficient	0.10081
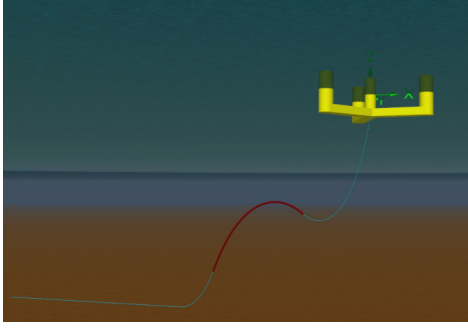
Fig. 4 Riser configuration (Blue line: bare part, red line: buoyancy part)

of the buoyancy module to determine the optimal riser configuration. Initial riser configuration conditions were referenced from Rentschler et al. (2019), where the total length of the riser (l_{total}) and the horizontal distance at both ends of the riser were set to 2.8 times and 2 times the water depth (h), respectively. The length ratio between the upper bare section and the buoyancy module section was set to 0.25 of the total riser arc length. In this study, the total arc length of the riser and the connection locations at both ends were fixed, and optimization was performed on the position and length of the buoyancy module. Detailed riser specifications are provided in Table 3, and the lazy wave riser is shown in Fig. 4. The red part in Fig. 4 indicates the buoyancy module. The representative element length of the mooring line and the riser was set to 10 m, with the element length gradually shortened near each boundary condition to minimize numerical errors.

3.3 Environmental Conditions

The design environmental conditions were established assuming the installation of a FOWT for green hydrogen production near Uldolmok in Uljin, South Korea. The conditions were based on the International Electrotechnical Commission's (IEC) report on design requirements for FOWTs (IEC, 2019), applying the operating condition DLC 1.1 with maximum wind speed, and the extreme load condition DLC 6.1. The operating condition was based on a maximum wind speed of 25 m/s at the hub of this 15-MW wind turbine, and the significant wave height and peak period at this wind speed were calculated using wind speed–wave height distribution tables. Additionally, the current speed induced by wind was calculated and applied based on DNVGL-OS-C205 (DNV GL, 2021c) (Eq.(7)), as follows:

$$V_{c,surf} = 0.03\, V_{w,1H,10m} \tag{7}$$

where $V_{c,surf}$ and $V_{w,1H,10m}$ denote the current speed at the sea surface and the hourly average wind speed at 10 m above the water surface,

respectively. For the extreme load conditions, the wave, current, and wind conditions with a 50-year recurrence period were referenced from Lee et al. (2023), and both the operating and extreme load conditions are summarized in Table 4. In these conditions, the wind, waves, and currents all act in the same direction. Typically, the wind speed criterion used in the design of floating structures refers to the speed at a height of 10 m above sea level, so the extreme wind profile was used to calculate the wind speed at the hub of the floating wind turbine as in Eq. (8) (DNV GL, 2021c; IEC TS 61400-3-2:2019, 2019).

$$V_w(z) = V_{w,hub}\left(\frac{z}{z_{hub}}\right)^{\alpha} \tag{8}$$

where V_w denotes the wind speed at a specific location (z), $V_{w,hub}$ denotes the wind speed at the hub location, and z_{hub} denotes the height of the hub above the water surface. The α values 0.14 and 0.11 were used for the operating and extreme conditions, respectively (DNV GL, 2021b; European Commission, 2015).

4. Numerical Analysis Results

4.1 Validation Test

In this section, the hydrodynamic performance of the floating platform under wave conditions with a white noise spectrum is analyzed and compared the open published results to validate the numerical modeling of the floating wind turbine. Comparing the results between them, the green hydrogen riser was not considered. Fig. 5 shows the incident wave spectrum and the response amplitude operator (RAO) of the floating platform. When waves are incident in the negative x-axis direction, without the influence of currents or wind, the time-domain motion equations (Eq. (1)) can be used to describe the global motion of the floating platform. In this study, the total analysis time was 3 hours. The time series data of the platform's global motion were transformed into a response spectrum using Fourier transformation, and then the incident wave spectrum (Fig. 5(a)) was applied for backward estimation of the motion RAOs (Fig. 5(b)). The time step in numerical analysis was set to 0.025 s. The estimated results generally matched those of Allen et al. (2020).

Based on the validated numerical modeling, the global motion of the floating platform was analyzed under two environmental conditions (Table 4). The directions of the waves, currents, and wind were all aligned in the positive direction of the x-axis. Irregular waves were generated using the Joint North Sea Wave Project (JONSWAP) spectrum, with the analysis time set to a storm duration of 3 hours (Fig. 6). Fig. 6(b) shows the incident wave spectrum reconstructed from the

Table 4 Environmental conditions (wave, wind, and current)

	Significant wave height, Hs (m)	Wave peak period, Tp (s)	Enhancement factor, γ	Wind speed at 10 m above mean water level, V_w (m/s)	Wind speed at the hub, $V_{w,hub}$ (m/s)	Surface current speed, $V_{current}$ (m/s)
DLC 1.1	6.20	12.40	1.0	17.11	25.00	0.46
DLC 6.1	8.34	13.1	1.7	30.68	41.33	1.69

(a) Wave spectrum

(b) Motion RAOs

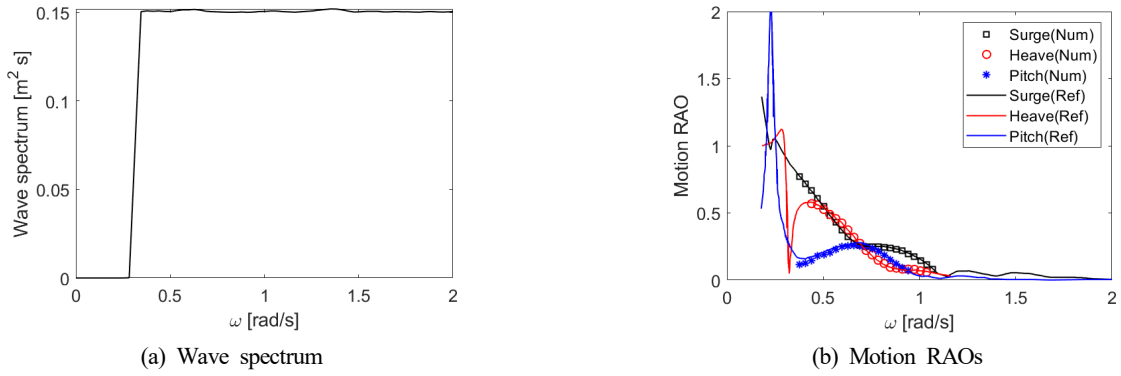**Fig. 5** Wave spectrum and motion RAOs compared with open published results (Allen et al., 2020)

(a) Incident wave time histories

(b) Wave spectrum

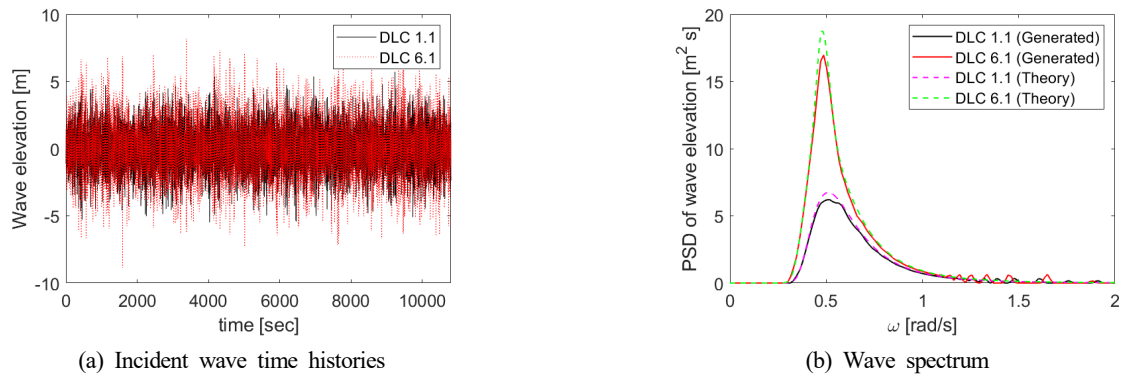**Fig. 6** Comparison of incident wave time histories and wave spectra under DLC 1.1 and DLC 6.1

(a) Time histories of surge motion displacement

(b) Time histories of heave motion displacement

(c) Time histories of pitch motion displacement

(d) PSD of surge motion displacement

(e) PSD of heave motion displacement

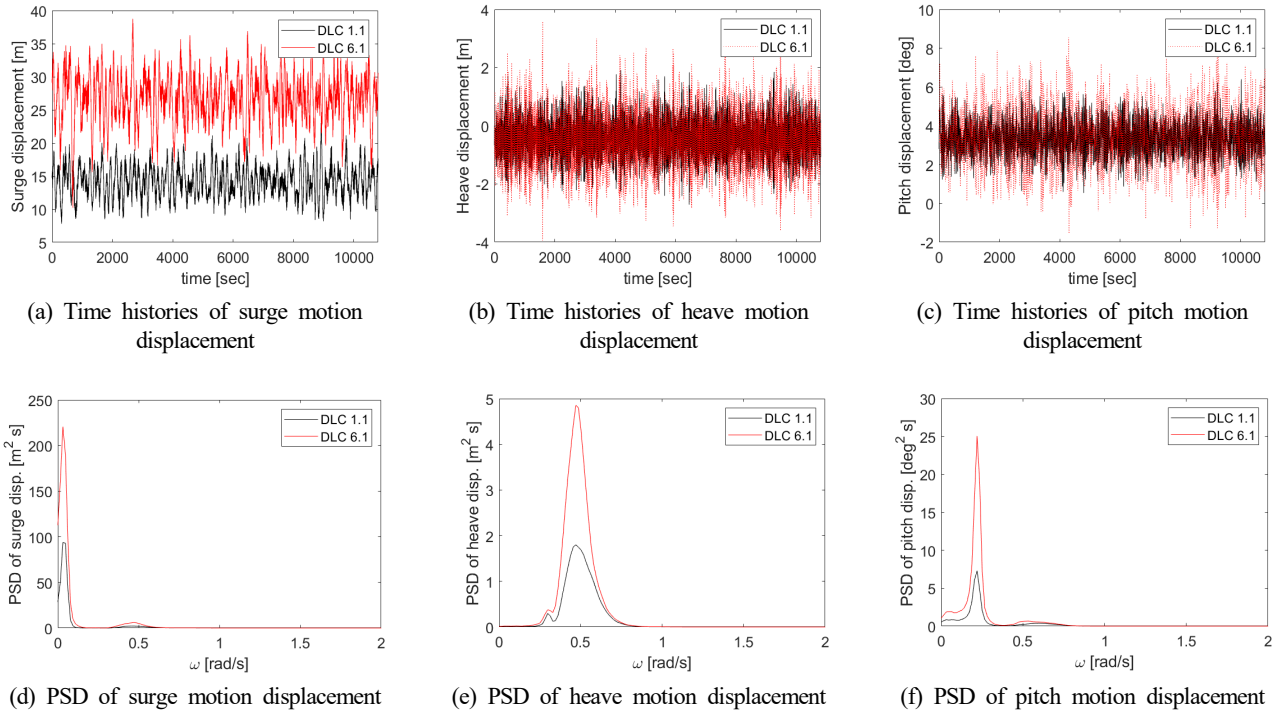(f) PSD of pitch motion displacement

Fig. 7 Time histories and PSDs of 3 degrees of freedom motion response (surge, heave, and pitch)

time series of Fig. 6(a), compared with theoretical predictions.

Fig. 7 illustrates the global motion of the floating platform under two environmental conditions. As the platform is symmetrical along the x-axis and incidence angle of the environmental load is in the positive direction of the x-axis, only three degrees of freedom (surge, heave, and pitch) were calculated. The response characteristics were examined by transforming the motion response spectrum through Fourier transformation. Due to the larger significant wave height, wind
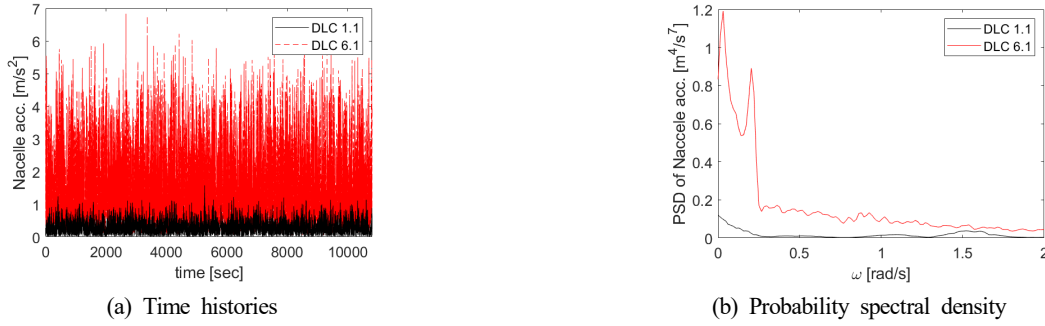
(a) Time histories

(b) Probability spectral density

Fig. 8 Nacelle acceleration and bending moment at the basement of tower

(a) Time histories of mooring line #1

(b) Probability spectral density of mooring line #1

(c) Time histories of mooring lines #2&3

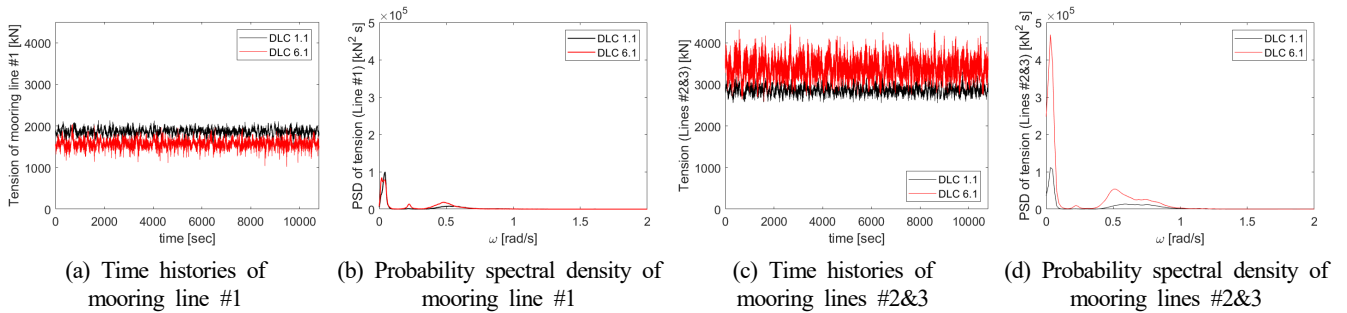(d) Probability spectral density of mooring lines #2&3

Fig. 9 Time histories and probability spectral density of line tension of mooring lines

Table 5 Mooring lines' natural frequency (rad/s)

	1st	2nd	3rd	4th	5th
Line #1	0.419	0.728	0.828	1.147	1.236
Line #2&3	0.437	0.812	0.867	1.217	1.298

speed, and current speed, DLC 6.1 showed the average position of the floating platform moving further in the positive direction of the x-axis compared to DLC 1.1. Surge motion appeared more pronounced at lower frequencies rather than wave frequency motion. Heave motion primarily showed a significant response at the peak wave frequency, while pitch motion was predominantly observed at the natural frequency. Overall, under DLC 6.1 conditions, higher significant wave heights resulted in greater motion responses compared to DLC 1.1.

Along with the three degrees of freedom behavior of the floating platform, the nacelle accelerations (Fig. 8) and mooring line tensions (Fig. 9) under two loading conditions were compared. Nacelle acceleration is directly related to the power production of the floating wind device. According to Boo et al. (2018), the nacelle acceleration under operating conditions should be less than $0.4g$ (= 3.924 m/s²). In this analysis, under operating conditions (DLC 1.1), a maximum nacelle acceleration of 1.5 m/s² was observed, meeting the design requirements. For extreme conditions (DLC 6.1), a maximum of approximately 7 m/s² was evident. Furthermore, in the nacelle acceleration's Power Spectral Density (PSD) shown in Fig. 8(b), low-frequency components below 0.3 rad/s appear under DLC 6.1 conditions, whereas components around 1.5 rad/s and below 0.3 rad/s were evident under DLC 1.1. The mooring line tensions (Fig. 9) are shown separately for mooring lines 1, 2, and 3, considering the platform's x-axis symmetry. As shown in Fig. 7(a), the average

position of the floating platform moved further in the positive direction of the x-axis under DLC 6.1 than under DLC 1.1. Consequently, mooring line 1 experienced a smaller static tension, while mooring lines 2 and 3 had greater static tension. Additionally, due to the relatively large motion responses of the floating platform under DLC 6.1 conditions, significant dynamic tensions also occurred. However, the maximum tension was approximately 4,500 kN, which is much smaller than the maximum allowable load of the mooring line (13,928 kN). The maximum allowable load is calculated based on a maximum allowable load of 22,286 kN considering a safety factor of 1.6 applied, based on the American Petroleum Institute standards (API, 2008). The PSD of the mooring line tension under extreme loading conditions reveals the behavior characteristics of the mooring line, with relatively large tensions evident at the natural frequencies of the surge, heave, and pitch motions. Importantly, the impact of the surge motion mode, characterized by low-frequency movement, was most significant on the mooring line tension. Table 5 indicates the natural frequencies of the mooring lines, showing that their impact was relatively minor.

4.2 Effect of Length of Upper Bare Section

In this section, the flexible riser for transporting green hydrogen associated with offshore wind power facilities is considered. Using previously verified numerical modeling of the floating offshore wind power facility, a lazy wave riser for hydrogen transportation was
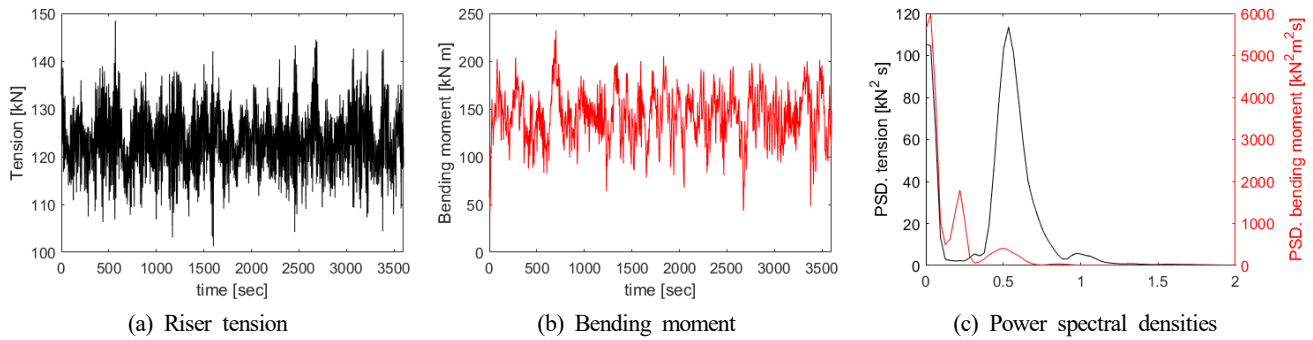
| (a) Riser tension | (b) Bending moment | (c) Power spectral densities |

Fig. 10 Time histories of riser tension (a) and bending moment (b) and their power spectral densities(c) (Arclength = 0 m)
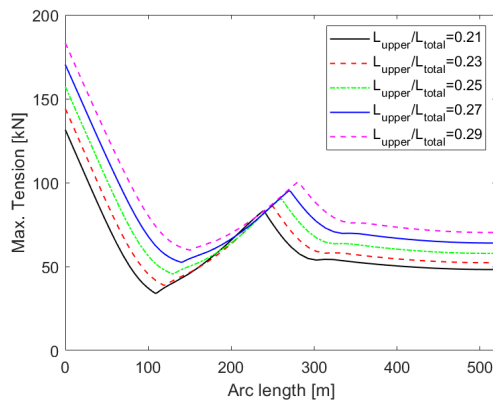
Fig. 11 Maximum riser tension with various kinds of upper bare section's length along the arc length
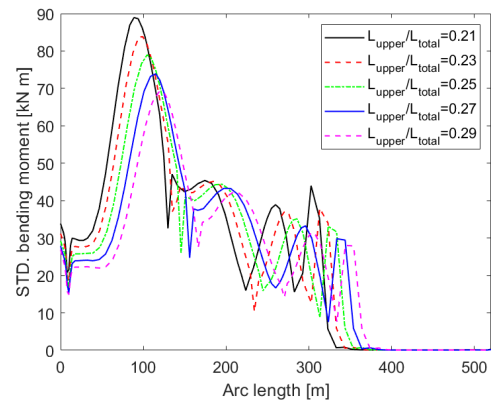
Fig. 12 Standard deviation of bending moment with various kinds of upper bare section's length along the arc length

applied, and a parametric study was conducted to determine the optimal riser profile. To achieve the desired lazy wave riser configuration, a buoyancy module was applied in the middle of the riser. This section estimates the impact of the length of the upper bare section of the riser, which refers to the portion from the floating platform to the start of the buoyancy module, without the module itself. Fig. 10 illustrates the tension and bending moment at the connection point between the riser and the floating platform. Here, the lengths of the buoyancy module and the upper bare sections corresponded to 0.25 of the total riser length, with environmental conditions set to DLC 6.1. The maximum tension and bending moment observed were approximately 148 kN and 230 kN·m, respectively. Analyzing the PSD of the tension and bending moment, it is found that the tension was significantly influenced by both the low-frequency motion and the wave frequency motion of the floating platform, while the bending moment was primarily affected by low-frequency motion. Consequently, to ensure the riser's safety, minimizing low-frequency motion is crucial.

Figs. 11 and 12 show the maximum tension and the standard deviation of the bending moment across the riser, based on the length of the upper bare section. The maximum tension can be used to assess the safety of the riser concerning its maximum allowable tension, while the standard deviation of the bending moment can estimate short-term fatigue damage. The tension in the riser is greatest near the floating platform and decreases as one moves away from it. The tension increases due to the partially acting buoyant force, and it tends

to decrease again once the buoyancy module ends where the buoyancy module begins. The overall increase in the maximum tension of the riser as the distance from the buoyancy module increases suggests that having a shorter upper bare section is advantageous for riser safety. Additionally, this demonstrates that the lazy wave riser is structurally safer compared to a catenary riser without the buoyancy module.

The standard deviation of the bending moment varies significantly depending on the presence of the buoyancy module. Notable changes in the standard deviation were observed at several critical points: the sag bending point before the start of the buoyancy module, the hog bending point within the buoyancy module, the inflection point after the buoyancy module, and the touchdown point of the riser. The maximum standard deviation occurred at the sag point within the upper bare section. When analyzing the effect of the length of the upper bare module, shorter lengths resulted in higher maximum values of the standard deviation of the bending moment. This is attributed to the sag bending point being located higher up, increasing the impact of waves near the water surface. While the buoyancy module can reduce fatigue damage at the touchdown point, an increase in fatigue damage at the upper part of the riser was observed. Additionally, small but somewhat discontinuous bending moments were noted at the connection points between the floating platform and the riser, as well as at the points where the buoyancy module begins and ends.

4.3 Effect of Length of Buoyancy Module Section

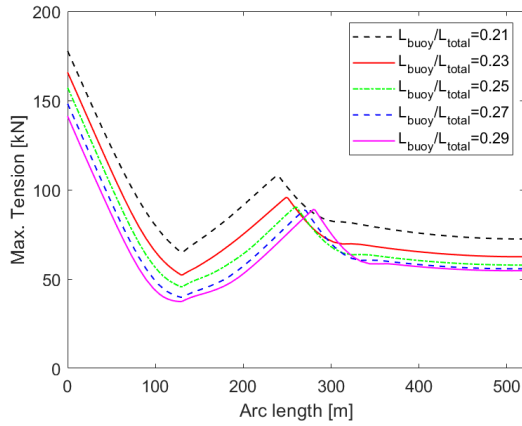In the previous section, the impact of the length of the upper bare

Fig. 13 Maximum riser tension with various kinds of buoyancy module section's length along arc length
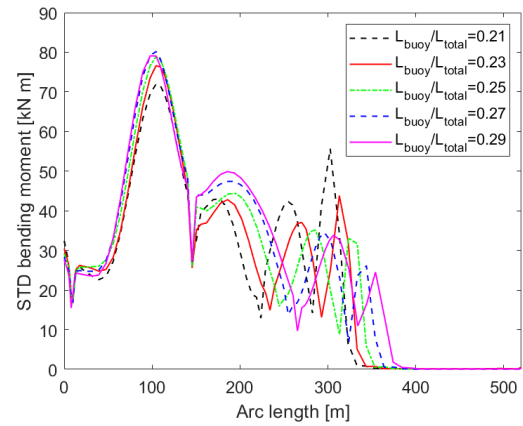

Fig. 14 Standard deviation of bending moment with various kinds of buoyancy module section's length along arc length

section was considered. This section focuses on the impact of the length of the buoyancy module section. The buoyancy module is installed starting at the quarter point of the riser's total length, and its length varies as 0.21, 0.23, 0.25, 0.27, and 0.29 times the total length of the riser. Figs. 13 and 14 show the maximum tension and the standard deviation of the bending moment across the riser, respectively, for different lengths of the buoyancy module section. As observed in Fig. 11, when there is no buoyancy module, the tension decreases as one moves away from the floating platform. When a module is present, the tension gradually increases as the distance from the platform increases. As the module length increases, the riser generally experiences more buoyant force, resulting in lower maximum tension. The standard deviation of the bending moment follows a similar trend as in Fig. 12. While the length of the buoyancy module section has little impact on the standard deviation of the bending moment in the upper part of the riser, longer lengths lead to a decrease in the standard deviation of the bending moment at the touchdown point. In terms of fatigue damage, increasing the length of the module is advantageous.

4.4 Response Surface Analysis

Next, based on the findings detailed in Sections 4.2 and 4.3, the effects of the lengths of the buoyancy module section and the upper bare section on the tension and bending moment were examined. A parametric study was conducted using five different lengths for the buoyancy module section (0.21, 0.23, 0.25, 0.27, and 0.29) and five different lengths for the upper bare section, presented through a 2D response surface analysis (Fig. 15). For each length condition, the maximum value of the tension (Fig. 15(a)) and the maximum value of the standard deviation of the bending moment (Fig. 15(b)) across the riser were compared. The study found that when the upper bare section is short and the buoyancy module section is long, the smallest maximum tension was observed, while the standard deviation of the bending moment was largest under the same conditions. Specifically, the maximum tension was lower with a longer buoyancy module section and higher with a longer upper bare section. However, the standard deviation of the bending moment was more significantly affected by the length of the buoyancy module section than by the length of the upper bare section, with shorter buoyancy module
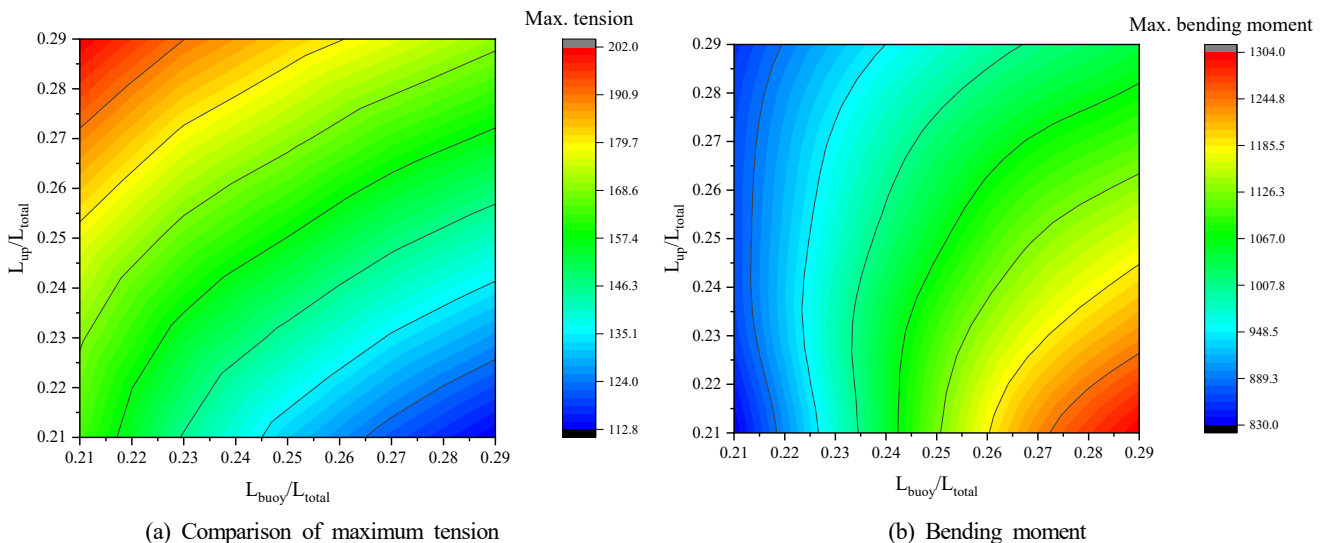

(a) Comparison of maximum tension

(b) Bending moment

Fig. 15 Comparison of maximum tension (a) and bending moment (b) of green hydrogen riser

sections showing lower standard deviation values. In conclusion, to ensure safety under extreme conditions and reduce fatigue damage, both the upper bare section and the buoyancy module section should be relatively short.

5. Conclusion

In this study, a parametric analysis was conducted on the lengths of the buoyancy module section and the upper bare section of a riser for a green hydrogen production base associated with a FOWT facility. A full coupled analysis of the FOWT, mooring lines, and riser was performed, and operating and extreme environmental conditions were assessed based on actual marine observation data from the Korean coast.

Initially, the validity of the numerical model was established by applying a white noise incident wave spectrum and calculating the motion response function for comparison. Motion characteristics were analyzed through the coupled analysis of the floating platform and mooring lines. Additionally, nacelle accelerations under operating conditions and mooring line tensions under extreme conditions were analyzed to confirm that this floating platform meets the design criteria. The verified numerical analysis model applied to the riser for transporting green hydrogen examined the effects of the lengths of the buoyancy module section and the upper bare section on the maximum tension and the standard deviation of the bending moment of the riser. The results indicate that as the length of the buoyancy module section increases, the maximum tension decreases, while the maximum tension increases with the length of the upper bare section. Also, shorter buoyancy modules are expected to cause less fatigue damage, with relatively little impact from the length of the upper bare section.

These findings provide useful information for the design and operation aimed at efficient integration between floating offshore wind turbines and green hydrogen production facilities and are expected to contribute to future research and industrial applications. This study is limited to the safety analysis of green hydrogen risers under extreme environmental conditions, performed under parked turbine conditions. For a thorough evaluation of riser fatigue damage, follow-up studies should consider dynamic turbine behavior, turbine control techniques, and turbulent wind flow.

Conflict of Interest

No potential conflict of interest relevant to this article was reported.

Funding

References

Allen, C., Viselli, A., Goupee, D. A., H., Gaertner, E., Abbas, N., Hall, M., & Barter, G. (2020). Definition of the UMaine VolturnUS-S reference platform developed for the IEA wind 15-megawatt offshore reference wind turbine technical report. http://www.nrel.gov/publications.

API. (2008). *API Recommended Practice* 2SK. *Design and analysis of stationkeeping systems for floating offshore structures* (3rd ed.)

Balli, E., & Zheng, Y. (2022). Pseudo-coupled approach to fatigue assessment for semi-submersible type floating offshore wind turbines. *Ocean Engineering*, *261*, 112119. https://doi.org/10.1016/j.oceaneng.2022.112119

Boo, S. Y., Stenffen, S., & Kim, D. (2018). Concept design of floating wind platforms of Y-wind and T-wind for southeast offshore of Korea. *Fall Conference of KORA Wind Energy Association,* 1016(DA2)_SE1_04. http://www.vloffshore.com/index_htm_files/1016_DA2_SE1_04_Concept%20Design%20of%20Floating%20Wind%20Platforms%20of%20Y-Wind%20and%20T-Wind.pdf

DNV GL. (2021a). *Position Mooring* (DNVGL-OS-E301).

DNV GL. (2021b). *Design of Offshore Wind Turbine Structures* (DNVGL-OS-J101).

DNV GL. (2021c). *Environmental conditions and environmental loads.* Norway (DNVGL-RP-C205).

Elsas, J. H., Casaprima, N. A. G., Cardoso, P. H. S., & Menezes, I. F. M. (2021). Bayesian optimization of riser configurations. *Ocean Engineering*, *236*, 109402. https://doi.org/10.1016/j.oceaneng.2021.109402

Eurek, K., Sullivan, P., Gleason, M., Hettinger, D., Heimiller, D., & Lopez, A. (2017). An improved global wind resource estimate for integrated assessment models. *Energy Economics*, *64*, 552−567. https://doi.org/10.1016/j.eneco.2016.11.015

European Commission. (2015). *Qualification of innovative floating substructures for 10 MW wind turbines and water depths greater than 50 m*. https://doi.org/10.3030/640741

European Commission. (2020). *Communication from the Commission to the European Parliament, the Council, the European Economic and Social Committee and the Committee of the Regions: A hydrogen strategy for a climate-neutral Europe.*

Heo, K., Park, H., Yuck, R.-H., & Lee, D. (2023). Numerical investigation of a floating-type support structure (Tri-Star floater) for 9.5 MW wind turbine generators. *Energies*, *16*(24), 7961. https://doi.org/10.3390/en16247961

Ibrahim, R. L., Huang, Y., Mohammed, A., & Adebayo, T. S. (2023). Natural resources-sustainable environment conflicts amidst COP26 resolutions: Investigating the role of renewable energy, technology innovations, green finance, and structural change. *International Journal of Sustainable Development and World Ecology*, *30*(4), 445−457. https://doi.org/10.1080/13504509.2022.2162147

International Electrotechnical Commission (IEC). (2019). *Wind energy generation systems - Part 3-2: Design requirements for*

floating offshore wind turbines (IEC TS 61400-3-2:2019). https://webstore.iec.ch/publication/29244

Jin, C., Lee, I., Park, J., & Kim, M. (2023). Dynamic behavior assessment of OC4 semi-submersible FOWT platform through Morison equation. *Journal of Ocean Engineering and Technology*, *37*(6), 238−246. https://doi.org/10.26748/KSOE.2023.030

Lee, K., Kim, H.-S., & Kim, B. W. (2023). A study on the global motion performance of floater and mooring due to arrangement of detachable mooring system. *Journal of Wind Energy*, *14*(2), 26−33. https://doi.org/10.33519/KWEA.2023.14.2.003

Li, X., Ji, H., Zhang, B., Liu, T., & Ye, W. (2016). Design of flexible riser for FPSO in South China Sea. *Proceedings of the 26th International Ocean and Polar Engineering Conference*, 109−116.

Martinez-Luengo, M., Kolios, A., & Wang, L. (2017). Parametric FEA modelling of offshore wind turbine support structures: Towards scaling-up and CAPEX reduction. *International Journal of Marine Energy*, *19*, 16−31. https://doi.org/10.1016/j.ijome.2017.05.005

Niranjan, R., & Ramisetti, S. B. (2022). Insights from detailed numerical investigation of 15 MW offshore semi-submersible wind turbine using aero-hydro-servo-elastic code. *Ocean Engineering*, *251*, 111024. https://doi.org/10.1016/j.oceaneng.2022.111024

Orcina. (2023). *OrcaFlex documendation*. https://www.orcina.com/resources/documentation/

Pham, T. Q. M., Im, S., & Choung, J. (2021). Prospects and economics of Offshore wind turbine systems. *Journal of Ocean Engineering and Technology*, *35*(5), 382−392. https://doi.org/10.26748/KSOE.2021.061

Pillai, A. C., Gordelier, T. J., Thies, P. R., Dormenval, C., Wray, B., Parkinson, R., & Johanning, L. (2022). Anchor loads for shallow water mooring of a 15 MW floating wind turbine — Part I: Chain catenary moorings for single and shared anchor scenarios. *Ocean Engineering*, *266*, 111816. https://doi.org/10.1016/j.oceaneng.2022.111816

Rentschler, M. U. T., Adam, F., & Chainho, P. (2019). Design optimization of dynamic inter-array cable systems for floating offshore wind turbines. *Renewable and Sustainable Energy Reviews*, *111*, 622−635. https://doi.org/10.1016/J.RSER.2019.05.024

Trapper, P. A. (2020). Feasible numerical analysis of steel lazy-wave riser. *Ocean Engineering*, *195*, 106643. https://doi.org/10.1016/j.oceaneng.2019.106643

Yu, M., Wang, K., & Vredenburg, H. (2021). Insights into low-carbon hydrogen production methods: Green, blue and aqua hydrogen. *International Journal of Hydrogen Energy*, *46*(41), 21261−21273. https://doi.org/10.1016/J.IJHYDENE.2021.04.016

Author ORCIDs

Author name	ORCID
Kim, Sung-Jae	0000-0001-9582-8983
Park, Sung-Ju	0000-0002-7129-8567